Fuel 300 (2021) 120836

Contents lists available at ScienceDirect

Fuel

journal homepage: www.elsevier.com/locate/fuel

Full Length Article

Correlative nano-spectroscopic imaging of heterogeneity in migrated petroleum in unconventional reservoir pores

Rebekah E. Simon [a,*], Samuel C. Johnson [b], Omar Khatib [b], Markus B. Raschke [b,*], David A. Budd [a]

[a] University of Colorado, Department of Geological Sciences, Boulder, CO 80309, USA
[b] University of Colorado, Department of Physics, Boulder, CO 80309, USA

ARTICLE INFO

Keywords:
Asphaltenes
Solid bitumen
Nano-mechanical properties
Nano-IR spectroscopy
Atomic force microscopy
Niobrara formation

ABSTRACT

Low permeability unconventional oil and gas resources may experience formation damage due to the emplacement of viscous petroleum in narrow pore throats during petroleum migration and production. The composition of such pore-clogging molecules remains under-characterized, as standard analytical techniques in organic geochemistry either lack the desired nano-scale spatial resolution with simultaneous chemical specificity, or require extraction and therefore averaging of the suite of compounds that make up bulk crude oil. A new correlative imaging technique with high spatial resolution is demonstrated for migrated residual petroleum in nanopores of Niobrara chalk samples. Imaging combines Infrared scattering-Scanning Near-field Optical Microscopy (IR *s*-SNOM) with nano-mechanical atomic force microscopy to map both chemical and mechanical properties at ~30 nm spatial resolution. These correlative images demonstrate that heterogeneity exists within emplaced petroleum *in situ* on the scale of hundreds of nanometers, visualized as clusters of petroleum having distinct adhesive forces. The chemical composition of these clusters remains ambiguous, but their geometry and mechanical properties may imply that they are phase-separated asphaltene preferentially associated with petroleum-attractive nano-domains on calcite pore walls. Despite outstanding challenges, correlative IR *s*-SNOM and nano-mechanical imaging offer a promising and novel analytical approach to understanding fluid behavior in nanoporous reservoir rocks.

1. Introduction

The development of low-permeability unconventional oil and gas resources is assisted by better comprehension of the micro-scale spatial heterogeneity of organic matter—sedimentary organic matter, solid bitumen, and migrated petroleum [1–3]—that constitute the subsurface unconventional petroleum system. Scanning electron microscopy of ion milled core samples has documented the general spatial distribution of those components (Fig. 1) in numerous unconventional petroleum systems worldwide [4–9]. However, the *in-situ* characterization of chemical and mechanical heterogeneity in residual migrated petroleum across individual pores that themselves are typically <1 μm in unconventional reservoirs remains a major challenge due to limitations of routine analytical approaches. Routine approaches to characterization of a petroleum system's organic components include chemical analysis of extracted petroleum, hydrous pyrolysis, and spectroscopic methods such as Fourier Transform infrared spectroscopy and Raman microscopy [1,10–14]. However, none of these techniques are suited to sub-micron scale analyses They either fail to preserve spatial relationships, or in the case of FTIR and Raman techniques, are compromised by mineral matrix effects and/or diffraction limits when high spatial resolution is desired. Consequently, *in-situ* analysis of migrated petroleum in natural samples remains vastly under-studied compared to larger, more easily analyzed sedimentary organic macerals and solid bitumen. Addressing the paucity of analysis is important, given the critical role spatial heterogeneity in organic matter of all types can play in determining the quality and value of an unconventional petroleum resource.

The vertical spatial scale of features in unconventional oil and gas reservoirs spans at least eight orders of magnitude, from pore throats measured in 10s to 100s of nanometers [15] to 10s of meters-thick reservoir bodies. Crude oil is compositionally heterogeneous at the reservoir scale [16], and heterogeneity can extend to the smaller pore

* Corresponding authors.
E-mail addresses: Rebekah.Simon@colorado.edu (R.E. Simon), Samuel.C.Johnson@colorado.edu (S.C. Johnson), omar.khatib@colorado.edu (O. Khatib), markus.raschke@colorado.edu (M.B. Raschke), budd@colorado.edu (D.A. Budd).

https://doi.org/10.1016/j.fuel.2021.120836
Received 29 November 2020; Received in revised form 27 March 2021; Accepted 7 April 2021
Available online 12 May 2021

scale via the distribution of asphaltenes, which are known to be a dominant element of solid reservoir bitumen [2]. Asphaltenes are a family of complex, highly polar polycondensed aromatic sheet-like molecules linked with aliphatic chains and naphthenic rings, and host transition metals, notably V, Ni, and Fe, and heteroatoms O, N, and S [17]. Individual molecules are 1 to 1.5 nm in size [18–20], but under natural reservoir conditions and/or during reservoir depletion, asphaltenes may segregate and precipitate into larger aggregates or domains [21,22]. If, and how much precipitation occurs depends on reservoir pressure, temperature, dissolved gas content, and the composition of the crude oil itself [23,24]. The precipitated asphaltene structures include nanoaggregates <10 nm in size [16,25], larger clusters of nanoaggregates, and still larger floccules [16,19]. Sizes of the larger structures are not well constrained and their stability over geologic time is uncertain, but the smallest flocs are at least 300 nm [16] and particle sizes up to 2 μm have been recorded [26]. In oils with high concentrations of asphaltene, bulk phase separation becomes thermodynamically favored [20].

Asphaltenes in solution and as precipitates are prone to deposition, either on mineral surfaces by adsorption, or by hydraulic trapping and plugging of pore throats [23,27–31]. The resultant formation damage reduces permeability up to 30% to 40% in laboratory studies [30,31] and as inferred from pore-network models [28]. Adsorption prevails in conventional reservoirs where throat sizes are much larger than the asphaltene structures, but deposition in pore throats becomes the increasingly dominant process as throat sizes approach asphaltene particle sizes [31]. Pore plugging by asphaltenes, changes in wettability, absolute permeability reduction, and even complete isolation of pores from the fluid-flow network [30] are potentially serious problems in unconventional reservoir pore systems where throats are similar in size to asphaltene structures. Though the theoretical understanding of asphaltene-induced formation damage has improved, predicting where it will occur in any reservoir remains challenging.

Recently, atomic force microscope (AFM) based scanning probe techniques have emerged with the potential to greatly enhance investigations of the *in-situ* chemical and physical character of organic materials, including sedimentary organic macerals, solid bitumen, and migrated, pore-filling residual petroleum. Infrared nano-imaging including Photothermal AFM [32,33] and IR *s*-SNOM [34–36] offer nanoscale spatial resolution and chemical specificity based on the detection of characteristic molecular vibrations in sample material [e.g., [37–39]]. Scanning peak force microscopy and peak-force infrared microscopy (PFIR) document sample surface mechanical properties at equally impressive spatial resolution [40].

Recent applications of IR nano-imaging to sedimentary organic matter and partially modified macerals (solid bitumen) in oil shale samples suggest differences in the chemical functional groups of different macerals [41–46]. Others observe nanoscale heterogeneity in the mechanical properties of different macerals based on PFIR [42] or peak force nano-mechanical measurements [47–50]. Only one recent study [44] has documented heterogeneity in migrated petroleum in unconventional reservoir samples, and then primarily to explore for thermal maturity indicators. However, no studies have yet paired multiple scanning probe techniques in correlative analysis of the potential chemical and mechanical heterogeneity in the migrated petroleum within the micro- to nano-scale pores between framework minerals (Fig. 1B) that are meters or more away from the primary organic matter from which it was derived.

This study performs correlative imaging of chemical and mechanical heterogeneity in migrated petroleum in the nano-scale pores of an unconventional reservoir (Niobrara Formation, greater Wattenberg Field, Denver Basin, Colorado, USA). Correlative imaging—combining IR *s*-SNOM and peak force imaging—provides a rich array of complementary data that may advance understanding of how complex chemical mixtures like crude oils and sedimentary organic matter behave in natural geological materials, and improve the efficiency of development for such resources in the future.

2. Materials and methods

2.1. Geologic samples

Fourteen rock samples were collected from three different cores cut through the B Chalk zone of the Niobrara Formation, in wells with thermal maturity indicators ranging from the onset of oil generation to wet gas generative (0.72, 0.96 and 1.08 $\%VR_o$). All three wells are located within the greater Wattenberg Field of the Denver Basin, and the samples come from depths ranging from 7020 to 7600 ft (2140 to 2317 m). The Niobrara is not a traditional clay-rich shale, but is intercalated calcite-rich chalks, marly chalks, and marls [51–55]. Because calcite mineral surfaces attract polar oil molecules while silicates and aluminosilicates remain water-wet, the mixed-lithology reservoirs of the Niobrara are optimal locations for petroleum heterogeneity to develop. Zhang et al. [56] reported pore-occluding petroleum liquids that they interpreted as asphaltenes on ion-milled samples of Niobrara chalk held under vacuum, which are also similar in appearance to asphaltene and solid bitumen imaged by others [9,57]. Core retrieval invariably alters the distribution and chemical stability of organic molecules within a pore network, but the nanoporous nature of the Niobrara likely prevents flushing of hydrocarbons $> C_{10}$ as they solidify during rapid depressurization [58,59]. It is thus assumed that the presence and geometric arrangement of any precipitated petroleum in the core samples is a reasonable approximation of their distribution at reservoir conditions.

Samples were cut from the cores as 1 cm × 1 cm × 3–5 cm blocks. A 3 mm-thick slice off the square top of each block was removed intact, and the broad face manually polished with either a sequence of loose

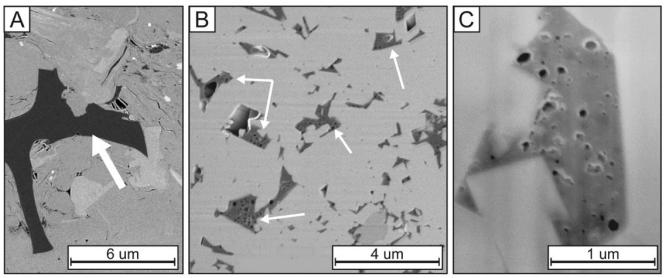

Fig. 1. Backscattered electron images of residual petroleum in ion-milled core samples of representative Niobrara B-chalk reservoir rock (images from study of Michaels and Budd, 2014 [82]; see also Canter et al [57] for similar imagery of the Niobrara reservoir rocks). A. Sedimentary organic matter maceral (white arrow). B. Intercrystalline pores in a chalk containing residual migrated petroleum (white arrows). C. Small circular pores (black) in the migrated petroleum occupying an intercrystalline pore. Light gray in all images is mineral matrix of the host rock. (For interpretation of the references to color in this figure legend, the reader is referred to the web version of this article.)

polishing grits slurried with deionized water or with diamond polishing pastes. Final polish using 0.050 μm water-based colloidal silica suspension removed any residue from the intermediary steps, and provided the sub-micron surface rugosity needed for AFM. Polished slices were sonicated in deionized water after the final polish.

2.2. ATR-FTIR on extracted total lipids

Total lipid extraction (TLE) was performed on the remaining portions of each sample block. Approximately 3g of each sample were powdered and solvent-extracted on a ThermoFisher Dionex Accelerated Solvent Extractor using a DCM:MeOH 9:1 vol solution at 100°C and 2000 psi (13.8 MPa). The resulting TLEs were dissolved in *n*-hexane, agitated, and chilled for at least two hours to allow asphaltenes to precipitate. The maltene fraction containing the saturated, aromatic, and resin fractions ("S", "A", and "R" of SARA; asphaltene being the final "A") of the extracted bitumen remained dissolved, and was pipetted off to be used for attenuated total reflectance FTIR (ATR-FTIR). Additional details for this sample preparation can be found in Boudinot et al. [60] and Simon [61].

FTIR spectra for asphaltene and maltene fractions of each extracted sample were acquired with a benchtop Cary-630 ATR-FTIR instrument with a diamond reflection element by summing 32 coadded scans at ~4 cm^{-1} spectral resolution between 400 and 4000 cm^{-1}. The spectra were collected from dilute solutions of each TLE fraction in a CS_2 diluent, and corrected for atmospheric interference during acquisition. Sample dilution was not controlled, so sample to sample comparisons of raw spectral intensity are not made. FTIR spectra are presented as percent transmittance. They were linear slope and offset baseline corrected and min–max normalized during data post-processing. No spectral smoothing was performed. Spectral features in transmission data appear as low light transmittance, while spectral features in IR *s*-SNOM data may be more ambiguous if chemical mixtures are compositionally complex.

FTIR spectra were fit in three regions using a non-linear least squares minimization function over a linear sum of Gaussians. The regions include 2820–3050 cm^{-1}, which is the aliphatic C–H stretching range; 1540–1630 cm^{-1}, which is the aromatic C–C/C=C stretching range; and 1655–1755 cm^{-1}, which is the C=O carbonyl/carboxyl stretching range. Linear baseline flattening was performed on a case-by-case basis prior to fitting—some spectra had severely tilted baselines because of overlapping features adjacent to the fit window, while others' baselines were relatively flat if those adjacent features were small. The resultant peak areas were used to calculate A- and C-factors for the extracted asphaltene and maltene fractions, which are useful proxies for the molecular reorganization that occurs during petroleum maturation and migration [13]. The equations for the two factors were adapted from those of Ganz and Kalkreuth [13] in order to accommodate the data regions available. The A-factor (defined herein as the sum of areas for peaks at 2850, 2870, 2920 and 2950 cm^{-1} divided by the sum of areas for peaks at 2850, 2870, 2920, 2950, and 1600 cm^{-1}) represents the proportion of aliphatic versus aromatic molecules. The C-factor (defined herein as the sum of areas for peaks at ~1700, ~1720, and ~1736 cm^{-1} divided by the sum of peak areas at 1700, 1720, 1736, and 1600 $cm^{-1)}$ is the proportion of carbonyl/carboxyl moieties relative to carbon–carbon bonds. The positions of fitted peaks along the wavenumber axis were also used to provide reference points for nano-scale IR *s*-SNOM imaging, both in term of appropriate laser focal points and of expected spectral features.

2.3. IR s-SNOM imaging of in-situ petroleum

Of the fourteen samples prepared for analysis, two were prioritized for extended analysis using infrared scattering-scanning near-field optical microscopy (IR *s*-SNOM)—a wet gas mature sample from Well O, and an oil mature sample from Well N. Infrared scattering-scanning near-field optical microscopy achieves nanometer spatial resolution through nano-scale localization of IR radiation focused onto the apex of a metalized atomic force microscope tip [35] (Fig. 2A). The infrared vibrational near-field interaction between the optically-excited tip and underlying surface provides spectroscopic information with a spatial resolution that is limited by the radius of the tip apex (~10–30 nm) rather than the wavelength of the IR light (~5–10 μm). The AFM is operated in tapping mode with tip oscillation frequency ω_t and the tip-scattered light is detected with a mercury cadmium telluride (MCT) detector. The near-field signal is discriminated from the far-field background by demodulating the tip scattered light at higher harmonics of the tip tapping frequency. Using broadband IR laser radiation, the nano-localized complex-valued spectra of the material are obtained by Fourier transform spectroscopy [35,36,62]. Tips were gold-coated silicon cantilevers for nano-IR with a 30 nm apex radius, a 300 kHz resonant frequency, and a 26 N/m spring constant. Tunable mid-IR light was generated by difference frequency generation (DFG) of signal and idler beams from a 40.53 MHz Optical Parametric Oscillator (OPO) with an output power of 35 mW. The DFG light was reliably tunable from 4.5 μm (2200 cm^{-1}) to 15 μm (666 cm^{-1}). See Supplementary Information for additional instrument details.

Complex-valued interferograms were apodized and subsequently Fourier transformed, producing near-field amplitude and phase spectra (the latter of which are qualitatively comparable to ATR-FTIR spectra) with a spectral resolution of ~4 cm^{-1}. All IR *s*-SNOM nano-spectroscopy data were referenced to gold to normalize the effects of signal attenuation through the focal path, and phase spectra were line corrected across the bandwidth of each laser tuning window. Topography and white-light second-harmonic near-field intensity image channels (see Supplementary Information) were acquired over 5–10 μm fields of view with 30 nm pixel resolution, and with the laser tuned in 100 cm^{-1} increments between 1400 and 1800 cm^{-1}. This range was selected based on the FTIR spectral features observed in asphaltene and maltene extracts, under the assumption that the gross family of chemical moieties present in extracted bitumen would correlate to imageable functional groups *in-situ* using IR *s*-SNOM. The range has close proximity to a major calcite resonance at ~1435 cm^{-1} and encompasses a number of resonance ranges known to represent nitrogen, sulfur, and oxygen moieties, which are concentrated in asphaltenes, between 1500 and 1800 cm^{-1}. This laser range is expected to have limited interference from other minerals that may visually mimic small residual petroleum filled pores such as aluminosilicates and from siloxane environmental contaminants (a family of polymers also used to manufacture the metalized tips) which have resonances between 1150 and 1300 cm^{-1}. Stronger resonances, such as C–H modes near 3000 cm^{-1}, are present in all TLE fractions and are thus unsuitable for imaging heterogeneity, though variability in this region may be of interest for evaluating mixed organic matter sources or thermal maturity (e.g., [44]). Additionally, experimental constraints including laser bandwidth and power made targeting those resonances and resonances <1000 cm^{-1} impossible. The noise floor for the second harmonic channel was typically between 3 and 8 μV, and this harmonic typically represents the best tradeoff between far-field background suppression and signal-to-noise ratio.

2.4. Nano-mechanical imaging of in-situ petroleum

Nano-mechanical imaging experiments (Fig. 2B) measure and derive sample topography, adhesive force, rigidity, deformation potential, and energy dissipation based on the force–displacement relationship between the sample and the tip [e.g., [38,63]]. Imaging was performed using the same tips as in IR *s*-SNOM. Each tip was force-calibrated to a germanium test sample, with the size of the tip apex determined by a reference image on rough titanium dioxide. Measured and calculated parameters include topography, adhesion, a rigidity modulus (DMT Modulus) and its logarithm, deformation, and dissipation. These parameters were determined on a pixel-by-pixel basis using the attractive forces between the tapping tip and the sample surface (Fig. 2B). The

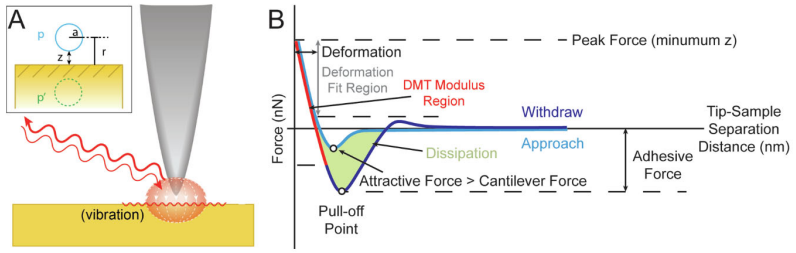

Fig. 2. A. Schematic representation of the AFM tip-sample interaction in IR *s*-SNOM (modified from Muller et al. [37]), where incident IR light is backscattered (red lines) by a nano-scopic volume. Inset shows a schematic diagram of the simple mirror dipole model for the near-field interaction, where the tip is represented by a polarizable sphere (p) which is mirrored at distance r in the sample (p′). B. Tip-sample force curve for nano-mechanical imaging based on near-field interaction over a full approach, contact, and withdrawal cycle of the tip to the sample surface, modified from Pittenger et al. [63]. Curves are color-coded to key regions and points by which nano-mechanical measurements of materials are made. (For interpretation of the references to color in this figure legend, the reader is referred to the web version of this article.)

resultant images were plane-leveled and minor tip artifacts removed using the open-source software program Gwyddion [64].

3. Results

3.1. ATR-FTIR on extracted petroleum

FTIR spectra for the extracted asphaltene and maltene fractions show a variety of strong resonances characteristic of aliphatic and aromatic C–H, C=O, C–C, and C=C bonds [65], both within the 1400–1800 cm^{-1} frequency range of interest for nano-analyses (Fig. 3) and over the full mid-IR range of 400–4000 cm^{-1} (Supplemental Data Figure S1 and Table S1). Asphaltenes are particularly characterized by the broad –OH and narrower C-O stretch of R-OH alcohols, as well as additional weak absorbances that may indicate C-O-C modes of alkyl aryl ethers [64]. Alas, many of these asphaltene specific modes are outside the identified range of interest for IR *s*-SNOM. Within the window of interest, a possible C–C pyrrolic nitrogen breathing mode, N-O stretch mode, or C=S stretch mode occurs in the asphaltene spectra at ~1513 cm^{-1} (Fig. 3). However, its origin is not definitive due to its possible attribution to other C–C ring modes, and its direct overlap with the C=S bond of the carbon disulfide solvent used to place samples on the ATR-FTIR window. As a result, the FTIR spectra of the extracted fractions are not sufficiently distinct to allow for their unique assignment and correlation with IR *s*-SNOM imaging. This is not completely unexpected, as only the saturate fraction of extracted bitumen should completely lack non C–H moieties, but it was mixed with the aromatics and resins during analysis. Differences in spectral intensity and feature position were too minor to identify separate fractions.

Despite the lack of fraction-defining modes, several differences in overall spectral character and geochemical ratios exist between asphaltenes and maltenes. The average total peak area that represents

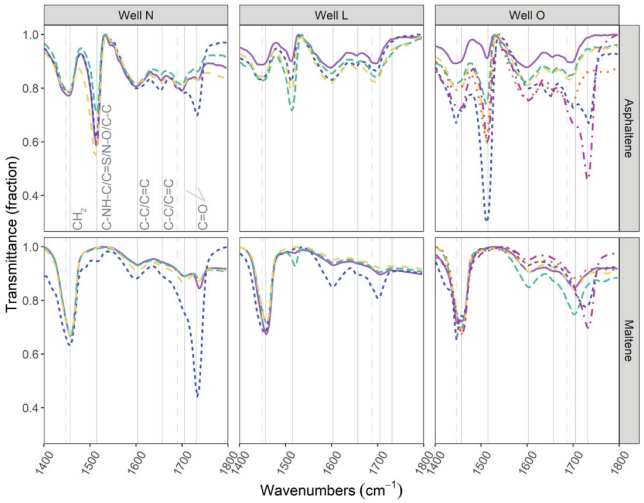

Fig. 3. FTIR spectral slices spanning 1400–1800 cm^{-1} for extracted asphaltene and maltene from the Niobrara B Chalk interval, separated by well. Colors and stippling indicate separate samples for ease of matching asphaltene and maltene pairs. Samples are arranged in order of increasing thermal maturity from left to right (Well N, % VR_o = 0.72; Well L, % VR_o = 0.96; Well O, % VR_o = 1.08). Light gray lines indicate prominent features in the data, and their possible interpreted functional groups are notated on the first panel. Minor shifts, shoulders and broadening (dashed gray) are apparent between some samples, such as the small feature at ~1435 cm^{-1} visible in the blue spectrum of Well O, which may be the result of varying proportions of multiple overlapping peaks, but do not fundamentally alter the interpreted functional groups present. (For interpretation of the references to color in this figure legend, the reader is referred to the web version of this article.)

simple hydrocarbons with less complex molecular structures is nearly twice as large in the maltene fraction than the asphaltene (Table 1), and peaks are generally better resolved in both the stretching and bending regions. The CH_2 bend at 1453 cm^{-1}, for example, is more symmetric and prominent in the maltene spectra, likely due to the increased fraction of C–H rich molecules and their relative structural simplicity (Fig. 3). This observation is supported by comparison of the A-factors between asphaltene and maltene TLEs: asphaltenes have lower A-factors than maltenes, indicating less aliphatic hydrogen relative to the available carbon atoms (Fig. 4) and therefore structurally more complex molecules.

Table 1
Fitted peak areas for FTIR peaks of interest, and calculated A- and C-factors. Aliphatic C–H includes peaks at roughly 2850, 2870, 2920, and 2950 cm^{-1}; Ring C–C includes the peak at roughly 1600 cm^{-1}; C=O includes peaks at roughly 1700, 1720, and 1736 cm^{-1}.

Type	Well	Aliphatic C–H	Ring C–C	C=O	A-factor	C-factor
Maltene	Well N_1	2860.41	42.38	174.38	0.99	0.80
Maltene	Well N_2	2456.15	79.22	966.46	0.97	0.92
Maltene	Well N_3	2874.20	41.53	103.45	0.99	0.71
Maltene	Well N_4	2800.34	59.42	113.25	0.98	0.66
Maltene	Well L_1	2858.20	34.16	47.94	0.99	0.58
Maltene	Well L_2	2585.77	153.27	154.78	0.94	0.50
Maltene	Well L_3	2552.16	41.70	46.66	0.98	0.53
Maltene	Well L_4	2627.64	25.66	36.12	0.99	0.58
Maltene	Well O_1	2576.76	127.99	260.92	0.95	0.67
Maltene	Well O_2	2665.28	18.13	128.03	0.99	0.88
Maltene	Well O_3	2829.42	32.61	105.33	0.99	0.76
Maltene	Well O_4	2556.89	29.84	678.09	0.99	0.96
Maltene	Well O_5	2190.61	42.92	126.49	0.98	0.75
Maltene	Well O_6	2176.89	23.81	429.58	0.99	0.95
Asphaltene	Well N_1	1558.36	208.98	190.95	0.88	0.48
Asphaltene	Well N_2	1478.06	196.76	560.95	0.88	0.74
Asphaltene	Well N_3	1859.65	194.88	202.92	0.91	0.51
Asphaltene	Well N_4	1069.66	165.06	82.39	0.87	0.33
Asphaltene	Well L_1	730.11	133.42	114.41	0.85	0.46
Asphaltene	Well L_2	1044.60	164.59	121.47	0.86	0.42
Asphaltene	Well L_3	1351.19	134.33	146.56	0.91	0.52
Asphaltene	Well L_4	976.53	190.27	166.65	0.84	0.47
Asphaltene	Well O_1	765.29	190.66	88.58	0.80	0.32
Asphaltene	Well O_2	954.61	196.88	100.69	0.83	0.34
Asphaltene	Well O_B3	807.94	202.28	114.26	0.80	0.36
Asphaltene	Well O_4	1883.38	242.55	1177.70	0.89	0.83
Asphaltene	Well O_5	807.67	120.19	76.65	0.87	0.39
Asphaltene	Well O_6	1550.75	142.05	642.10	0.92	0.82

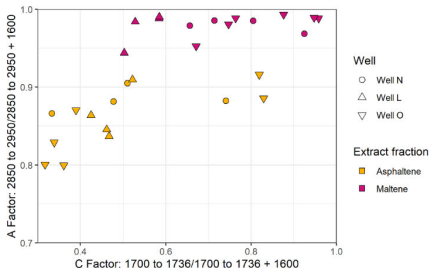

Fig. 4. A- and C-factors for extracted asphaltene and maltene fractions from Niobrara rock samples (Well N, %VR_o = 0.72; Well L, %VR_o = 0.96; Well O, %VR_o = 1.08).

In comparison, the aromatic and heteroatomic modes between 1600 and 1800 cm^{-1}, while present in spectra from both fractions, are generally stronger and more variable in asphaltene spectra. As an example, the C–C/C=C stretch at 1599 cm^{-1} is more prominent in the asphaltene fraction than the maltene fraction (i.e., nearly double the mean peak height relative to maltenes), but is broader with a more poorly defined peak shape. This may indicate a greater abundance of carbon rings or symmetric, conjugated alkenes, as is suggested by an average total peak area for C–C/C=C bonds in asphaltene that is nearly triple that of the maltene (Table 1). This interpretation is also supported by the A-factor relationship, which indicates fewer aliphatic bonds in the asphaltene fraction than the maltene, and may explain the C-factor relationship as well. The C-factor reflects the proportion of carbonyl/carboxyl moieties per available carbon. In the Niobrara samples, the range of C-factors is the same for asphaltenes and maltenes, but the average is overwhelmingly lower in the asphaltene, likely as a result of increased aromaticity. This variability in spectral features between 1600 and 1800 cm^{-1} makes the range well suited to chemically image the *in-situ* heterogeneity of petroleum in the Niobrara samples within the greater IR *s*-SNOM region of interest.

Between ~1550–1750 cm^{-1}, the asphaltene spectra display a noticeable baseline offset compared to the maltenes—often as much as 0.15 (15%) additional offset after baseline correcting the data over the total 400–4000 cm^{-1} range. This results in lower apparent amplitudes for some observed spectral features. These relatively broad, flat bands of enhancement across the spectra may suggest that asphaltene fractions have such significant chemical and structural complexity that a multitude of overlapping features from ring structures, heteroatoms, and sample three-dimensionality produces an unresolvable baseline in far-field infrared data [66]. Similar observations have been made when applying Raman spectroscopy to isolated asphaltene rings [67]. Recognizing this heterogeneity between asphaltene and maltene in far-field spectra, even if subtle, provides a framework for nano-scale analysis of *in-situ* petroleum.

3.2. IR s-SNOM images

Residual petroleum in pores is identifiable in the AFM images from their slightly recessed topographic expression relative to the surrounding mineral surfaces, and the clear angularity of pore boundaries that results from calcite crystal growth (Figs. 5 and 6). For laser center frequencies between 1400 and 1500 cm^{-1}, residual petroleum typically exhibits the weakest IR response across the field of view, while calcite minerals exhibit the strongest response due to the strong C-O stretch resonance of the carbonate group. Conversely, for laser frequencies of 1600–1800 cm^{-1}, residual petroleum has a stronger IR response compared to the mineral surfaces. Within individual pores, the IR *s*-

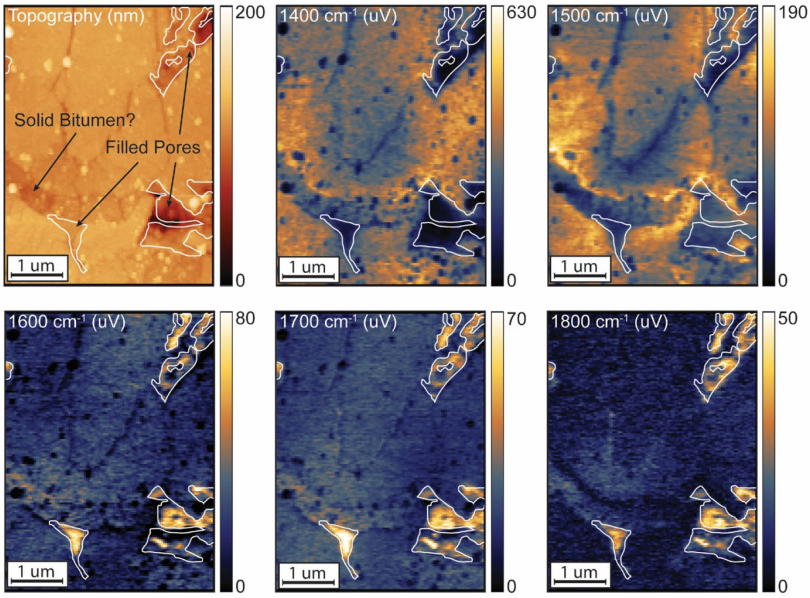

Fig. 5. Topography and near-field images for sample from Well N (0.72 %VR_o, oil generative) showing strong infrared response in residual petroleum within pores for 1600 to1800 cm $^{-1}$ images (outlined in white), and strong infrared response on calcite mineral surfaces for 1400–1500 cm $^{-1}$ images (light regions on topography). Images are scaled to appear similarly intense at each frequency, as the very strong contribution of the calcite resonance in the 1400 cm $^{-1}$ image prevents uniform scaling that can still highlight the residual petroleum in pores.

SNOM intensity appears homogenous, with marginal decreases near mineral interfaces that may be attributed to decreased tapping amplitude as the cantilever passes from mineral to residual petroleum domains.

The different FTIR spectral features observed and deconvolved in the extracted petroleum are not all apparent in the spatio-spectral *s*-SNOM imaging (Fig. 7A, B) even though the aggregate nano-resolved IR response of residual petroleum is strong over excitation windows covering 1600–1800 cm^{-1}. This is slightly surprising, as the gross family of molecules should be the same between *in-situ* migrated petroleum and extracted bitumen, even though the TLE process likely does not completely dissolve every bit of residual petroleum. However, spectral overlap may obscure less prominent features, especially in materials as complex as migrated petroleum. A pair of features possibly corresponding to carbon ring modes are visible at ~1625 and 1635 cm^{-1}, however, the strength of these features is partially dependent on the range over which the data were baseline corrected. Typically, prominent chemical moieties, as ring-bonded carbon is expected to be in residual petroleum, produce resonances that are more resilient across iterations of data post-processing. Accordingly, we interpret these features cautiously.

The consistently elevated phase response of most petroleum spectra (Fig. 7D, E) relative to the surrounding calcite indicates a strong broadband enhancement of the near-field signal, rather than the presence of any specific vibrational modes that could be correlated to functional groups in the migrated petroleum. Such broadband enhancement is consistent with the observed character of far-field asphaltene spectra over the same general spectral window, and corroborates the idea that chemical complexity within migrated petroleum obscures well-defined spectral features. Spectra collected over calcite exhibit a flat, featureless spectral amplitude and phase. This contrast is clearly documented by spectral comparison, which shows very high statistical similarity between point spectra across residual petroleum, and significant dissimilarity between the spectra from residual petroleum in pores and those of surrounding calcite (Fig. 7C). Therefore, IR *s*-SNOM allows for the nano-imaging with distinct contrast between residual petroleum and mineral matrix. Despite the challenges of interpreting spectral data for complex mixtures, these data suggest that IR *s*-SNOM can be a tool to successfully measure nano-scale, spatially registered chemically specific information from organic materials.

3.3. *Nano-mechanical images*

Nano-mechanical images show that residual petroleum in pores typically has high adhesive forces and material rigidity (Fig. 8). Adhesive forces inside residual petroleum are typically 2–4 times larger than the adhesive forces on the mineral surfaces. Differences of similar magnitude are observed for the log of the rigidity modulus. This modulus is a metric based on the local force plus adhesion, and it is likely that the rigidity modulus of the petroleum exceeds that of the surrounding calcite due to the adhesive force. Alternately, the higher rigidity modulus of the residual petroleum may be an unfortunate artifact of non-linear behavior at a very sharp tip apex. The absolute values vary, but adhesive forces in residual petroleum are commonly on the order of 30–60 nN and the log(DMT modulus) is around 1.5–2 log(GPa). The

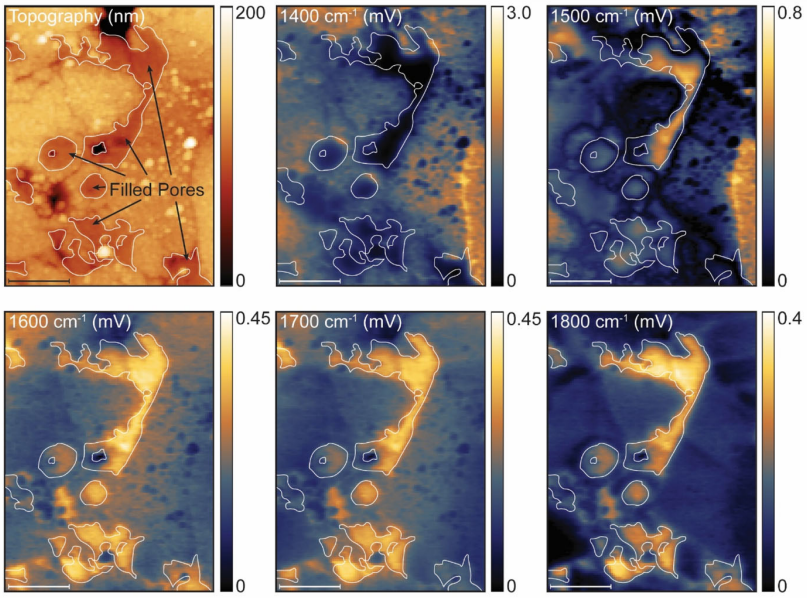

Fig. 6. Topography and near-field images for sample from Well O (1.08%VR_o, wet gas generative) showing strong infrared response in residual petroleum within pores for 1600 to1800 cm^{-1} images (outlined in white), and strong infrared response on calcite mineral surfaces for 1400–1500 cm^{-1} images (light regions on topography). Images are scaled to appear similarly intense at each frequency, as the very strong contribution of the calcite resonance in the 1400 cm^{-1} image prevents uniform scaling that can still highlight the residual petroleum. Scale bar (1 μm) presented as a line in the lower left of each image to prevent overlap with critical data.

energy dissipation does not exceed noise.

Nano-mechanical images suggest the existence of spatial heterogeneity on the 100s-of-nm scale inside pores filled with residual petroleum, as seen in the adhesion image (Fig. 8C), with higher rigidity and adhesion relative to the surrounding petroleum. These clusters of higher adhesion are, in some cases, more concentrated in one part of the pore relative to another (Fig. 8D). Assuming limited instrumental drift during acquisition, the clusters are commonly a few hundred nanometers in diameter. Surface features of similar scale are also observable on the calcite mineral surfaces, despite the overall magnitude differences in measured mechanical properties between mineral and petroleum in pores.

4. Discussion

4.1. Comparing Nano-scale and bulk geochemical results

Liquid petroleum undergoes a number of physical and chemical transformations during maturation and migration. Key among these are the increase in proportion of structurally complex, carbon-rich ring structures, and the adsorption of polar molecules to mineral surfaces [68]. Both the far-field FTIR data collected from lipid extract fractions and near-field IR *s*-SNOM images reflect higher aromaticity of residual petroleum in the samples analyzed. The FTIR-derived A-factor of the asphaltene fraction decreases with increasing thermal maturity: Well N (%VR_o = 0.72) has the highest average A-factor indicating less aromaticity (0.883), and Well O (%VR_o = 1.08) has the lowest, indicating more aromaticity (0.850). A proxy for the A-factor for the near-field IR s-SNOM data is generated by dividing the 1400 cm^{-1} image (the bending region for C–H bonds, as opposed to the stretching region used to calculate the A-factor for FTIR) by the sum of the 1400 and 1600 cm^{-1} images. The results (Supplemental Data Figure S2) show the residual petroleum in pores from the Well N sample have an average estimated A-factor of 0.825, while the average estimated A-factor for residual petroleum in pores from the Well O sample is 0.787. Though instrumental drift, laser realignment, and an eight-hour total scan time prevented the collection of spectral data at a controlled series of points across the entire 500 cm^{-1} window of interest for IR *s*-SNOM, this approximation corroborates the greater thermal maturity trends observed in the far-field data.

Non-parametric Kruskal-Wallis and post-hoc pairwise Wilcox tests demonstrate that about half of paired pore comparisons in each IR *s*-SNOM field of view have statistically significant differences in A-factors (Supplementary Tables S2 and 3). Unfortunately, neither the clear sample-to-sample trend in aromaticity nor the pore-to-pore statistical variation translate into visible intra-pore spatial heterogeneity in A-factor maps (Figure S2). Jubb et al. had success in documenting lateral spatial variability in A- and C-factors using AFM-IR analyses of solid bitumen [44]. Their scale of investigation was significantly larger than in this study as they calculated A- and C-factors over 5 and 20 μm wide regions. Jubb et al. [44] also used a quantum cascade laser, which has an extremely narrow bandwidth. This minimized the contribution of intensity from overlapping peaks that prevents the recognition of visible chemical heterogeneity in this study. Because the IR *s*-SNOM images in

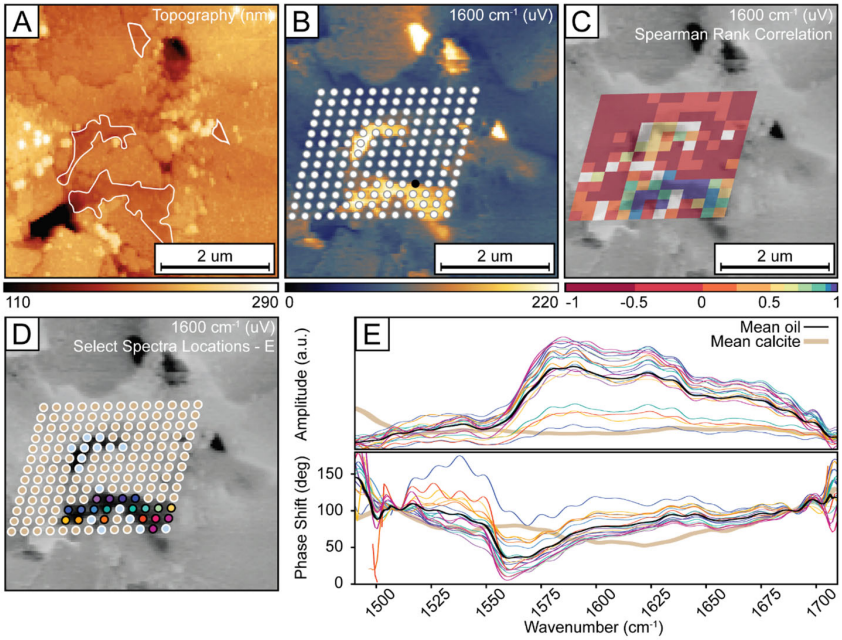

Fig. 7. Spatiospectral array for center frequency of 1600 cm^{-1} on the wet gas-generative sample from Well O (1.08 $\%VR_o$). A) AFM topography image showing residual petroleum in pores of interest (outlined in white), vacant pores (black) and calcite (yellows). B) Near-field intensity image, with the locations of array points overlain and corrected for sample drift. C) Near-field intensity image in grayscale overlain by the Spearman Rank correlation metric calculated using the spectrum at point 127 (an arbitrarily selected point on residual petroleum, black on panel B) at the 95% confidence interval. Cool colors indicate a positive correlation between the residual petroleum spectrum and the spectrum at point 127. Warm colors indicate a negative correlation between the residual petroleum spectrum and the spectrum at point 127. White blocks were not statistically significant, and are often located on transitions between residual petroleum and mineral. D) Locations of residual petroleum point spectra. Colors correspond to line colors in panel E; blue and tan dots correspond to points on the pore margin and calcite respectively and are not graphed. E) Amplitude and phase spectra for residual petroleum filled pores, normalized to a gold reference, showing broad similarity between residual petroleum spectra with high correlation coefficients. Black and tan lines are mean spectra for residual petroleum and calcite, respectively. (For interpretation of the references to color in this figure legend, the reader is referred to the web version of this article.)

this study were created with a broadband light source, they represent aggregate spectral intensity for any resonances in the ~150 cm^{-1} window surrounding each laser center position. Consequently, shifts in proportion between peaks residing close to each other are not visibly resolvable. Future IR s-SNOM workers may find more success evaluating chemical heterogeneity across pores filled with residual petroleum using a narrowband light source.

The adsorption of polar molecules to mineral surfaces during migration is the second major transformation that occurs during petroleum migration [69,70]. In particular, oxygen-bearing moieties are expected to occur largely in the liquid petroleum phase compared to the modified sedimentary organic matter, but they are also strongly polar and tend to adsorb onto mineral surfaces near the point of expulsion. Jubb et al. used to AFM-IR to document a systematic loss of carbonyl groups in solid bitumen across a centimeters-long transect from a source rock sample to a reservoir rock sample in the Stonewall Formation [46], and interpreted that trend to adsorption of polar molecules along that short migration path. In a separate study, Jubb et al. also used AFM-IR on solid bitumen in Eagle Ford Formation reservoir rock, and noted that C-factors were relatively low, and showed spatial variability across fields of view [44]. They attributed these observations to adsorption of oxygen-bearing moieties during migration as well.

In the Niobrara, there is also evidence for sedimentary organic matter-rich marls alternating at the centimeter scale with porous chalk containing migrated petroleum [57]. However, migration of petroleum over many meters also occurred from the underlying sedimentary organic matter-rich C marl into the B chalk [71]. The latter migration pathway may imply that a majority of C-O/C=O bearing molecule have effectively separated from the bulk petroleum prior to emplacement in the reservoir samples, if adsorption is happening at the spatial scale of Jubb et al. [46]. This could explain why relatively low C-factors were calculated from the asphaltenes of extracted Niobrara residual petroleum, and why those C-factors all occupy roughly the same range (~0.35–0.8) despite the differing sample thermal maturities. The much higher C-factor in the maltene extracts likely reflects a lack of aromatic molecules rather than a significant increase in carbonyls/carboxyls. This interpretation would also be consistent with the wide variability in C-factors between and within Jubb et al.'s Eagle Ford samples, which is encouraging as the Eagle Ford is lithologically comparable to the Niobrara.

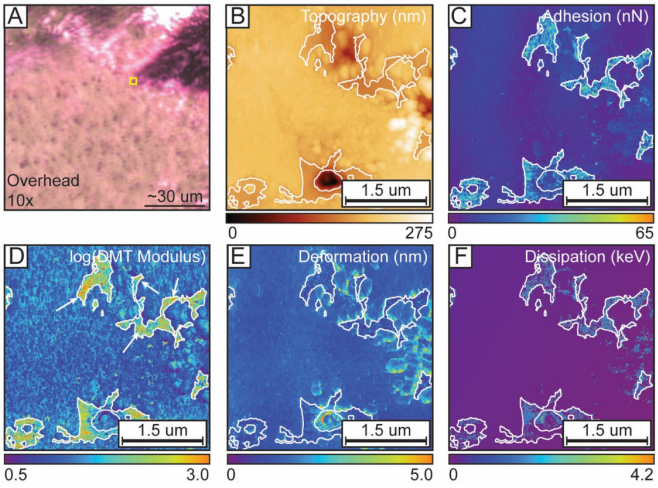

Fig. 8. Example of nano-mechanical results on residual petroleum in pores from the Well O sample (1.08 %VR_o). Pores containing residual petroleum are outlined in white. A) The overhead microscope image showing the calcitic peloid that hosts the residual petroleum-filled pores in B-F (yellow square beneath black cantilever point). Based on analogous SEM imagery such as Fig. 1, the dark spots within the peloid are likely empty nanopores. The top of the field of view contains a shadow from a piece of the instrument housing. B) Topography image of a ~4 μm square field of view. Yellow is calcite, darker yellow brown is residual petroleum, black is open pore. C) Adhesive force image showing high adhesive forces on residual petroleum surfaces. D) Image of log(DMT Modulus), a rigidity measurement based on the load force plus adhesion, showing high rigidity values of residual petroleum in pores (orange clusters indicated by white arrows) and nano-domains on calcite (blue mottling). E) Deformation image showing very little difference in deformation between residual petroleum and mineral. F) Dissipation image, uninterpreted due to poor signal to noise. (For interpretation of the references to color in this figure legend, the reader is referred to the web version of this article.)

It is important to acknowledge that the C-factors in this study come from extracted petroleum, while Jubb et al. analyzed both the Stonewall [46] and Eagle Ford [44] organics at the nano-scale. Unlike for the A-factors, a qualitative C-factor image was not calculated for the IR s-SNOM samples in this study. Due to the bandwidth of the laser windows in the IR s-SNOM analyses, it is possible that carbon-ring resonances used to calculate the denominator of the C-factor contribute to the aggregated signal intensity of the 1700 cm^{-1} image that would constitute the C-factor numerator, and vice versa. However, the patterns observed in C-factors from the extracted petroleum are still consistent with established petroleum systems theory [68–70] and with both of Jubb et al.'s previous nano-scale interpretations of carbonyl loss along migration paths.

4.2. Documenting the petroleum system at the Nano-scale

Overall, IR *s*-SNOM images clearly show nano-resolved residual petroleum and calcite domains over laser frequencies that stimulate well-understood petroleum molecule moieties like carboxyl groups and carbon ring structures (1600–1800 cm^{-1}, Figs. 5 and 6). These results are consistent with literature, including both studies on solid bitumen described above [44,46], and the results of the few nano-scale studies undertaken on organic macerals [41,45,72]. For example, Hao et al. observed broad, low-amplitude spectral features on the surface of macerals using ultra-broadband synchrotron infrared nano-spectroscopy, which allowed them to distinguish organic material from the surrounding mineral matrix [72]. Images from this study are even more striking, showing strongly responsive migrated petroleum in sharp contrast to non-responsive calcite mineral faces over a much smaller spatial scale.

Results from this study also align with literature (described below) that documents significant chemical complexity in sedimentary organic matter; however, in this study, the chemical complexity does not translate to visible spatial heterogeneity in migrated petroleum within pores. Spatially registered IR spectra in this study show spectral similarity across nanopores (Fig. 7E), but the broadband enhancement of each individual spectrum suggests overlapping peaks from numerous unique molecules—one mark of a complex mixture. Broadband enhancement is consistent with the far-field response of extracted petroleum (Fig. 3), with Jubb et al.'s recognition chemical complexity over tens-of-microns regions of Eagle Ford solid bitumen via a wide spread in A- and C-factors [44], and in macerals and solid bitumen from the Stonewall Formation at C=O and C–H regions [46]. Additionally, the overall spectral similarity of migrated petroleum in this study aligns with Yang et al. [41], who documented spectral variability between organic macerals from the New Albany shale at the C–H stretch frequency range, but saw relative homogeneity within individual inertinite and bitumen particles. Results from Jubb et al. [45] also demonstrated that intertinite, a type of woody maceral, in the Eagle Ford was relatively homogenous at the nano-scale.

All of these results demonstrate the utility of chemical imaging at the nano-scale. However, they also imply that measuring spatial heterogeneity requires distinctly different chemical entities that do not overlap, and that some analytical tactics may be of limited utility when analyzing residual migrated petroleum in closely space reservoir pores due to their bandwidth and the irreducible complexity of organic materials in such samples.

4.3. Documenting heterogeneity with correlative imaging

Despite the challenges of spectroscopically identifying chemically distinct sub-populations in a given pore, this study does demonstrate that correlative images of nano-mechanical data over regions filled with residual petroleum that has strong broadband enhancement from IR *s*-SNOM provides a targeted approach to coupled data collection. The results also suggest that differences in mechanical properties do exist inside pores filled with residual petroleum. Those variabilities appear to define small clusters of more adhesive phases that could indicate asphaltene precipitates. Critically, the clusters are similar in character to observed nano-domains on macerals [47], and appear morphologically similar to clusters of migrated petroleum imaged in other unconventional materials [29]. The character of these clusters is also consistent with experimental studies on exsolved petroleum. Synthetic crude oils with controlled proportions of asphaltene show that asphaltene-rich oils

are more mechanically rigid than low asphaltene oils [73]. Similarly, nano-mechanical measurements of several road bitumens have adhesive forces that are typically between 10 and 45 nN, energy dissipation typically between 1 and 5 keV, and deformation typically <1.5 nm [74,75]. The values of the clusters observed in nano-mechanical images from the Niobrara samples in this study are similar.

Current understanding of Niobrara reservoirs in the Denver Basin, including evidence from producing wells [58] suggests that phase segregation occurs during primary migration and production, leaving asphaltene distributed heterogeneously throughout the reservoir. The consistency between the mechanical properties of observed clusters in nano-mechanical images and known asphaltenes supports the inference that the clusters are precipitated asphaltene. This interpretation does not demand any specific spatial distribution for the clusters, as precipitates are likely to adsorb, behave as colloids, or sink within pores depending on their density and polarity. Alternatively, the clusters may reflect complex interactions between migrating petroleum and nano-domains on the calcite mineral surfaces, such as those identified on coccolith fragments at the 10s-of-nanometers scale [76]. Intrinsic variability in hydrophobicity associated with coccolith fragments may serve as a natural template for polar and non-polar molecules to separate during petroleum migration through chalks, even if P-T conditions did not facilitate precipitation of solid asphaltene floccules. Cluster-like thin films of adsorbed asphaltene would likely be sufficient to cause formation damage—especially where asphaltene-attractive nano-domains occur within narrow pores or throats, and especially if they serve as nuclei for asphaltene precipitates or micelle development as the reservoir fluids evolve through production.

The latter interpretation is supported by the spatial scale of the clusters in this study, which are both consistent with the scale of nano-domains identified on coccolith calcite [76] and are internally consistent with the size of small surface features visible on the calcite surfaces of the Niobrara samples analyzed (Fig. 8D). The clusters are slightly smaller than imaged petroleum spherules in other chalky unconventional materials [29], but the overall morphological similarity and abundance may imply the same formation mechanism, with cluster size controlled by the nano-domains particular to any given species of coccolith. Thus, nanomechanical images demonstrate that the geometry of the highly adhesive clusters in the residual petroleum may link to local zones of charge on calcite surfaces, an intrinsic property of the Niobrara chalk reservoir rock.

4.4. Challenges of Nano-imaging

Detecting chemical heterogeneity in the form of large asphaltene precipitates in near-field IR *s*-SNOM (or AFM-IR) would be facilitated if a spectral peak unique to asphaltene could be identified and easily mapped across pores. Without a distinguishing asphaltene spectral peak or a stronger contrast in molecular ratios, the IR *s*-SNOM analyses cannot differentiate asphaltene from maltene even if the former had precipitated and aggregated into large structures. Further, as other studies have shown that asphaltene precipitates accumulate on mineral surfaces or in pore throats [23,27,28,30,31], tip-mineral-oil interface complexities may also inhibit the detection of chemical heterogeneity where it is spatially most likely to occur.

Systematic study of the effect of different sample preparation methods of organic macerals and migrated petroleum is also warranted, as high-quality IR *s*-SNOM and nano-mechanical data are contingent upon a sample surface free of polishing artifacts or contaminants. Prior workers have attempted to use pressed powders [42], polished epoxy mounts [43–46], and polished whole rock prepared as in this study [41,72]. However, few have considered the impacts of their sample preparation techniques on analytical results, and one noted that their sample preparation procedure likely had negative impacts on their analytical results [42]. Alternative methods that warrant investigation include preparation with low energy ion beams [e.g., [47]]. This study opted not to prepare the samples under an ion beam because the localized heat on the milling surface can generate both chemical and physical artifacts unless tightly controlled [77–81]. The water-based polishing solution was comparatively unlikely to significantly disturb migrated organic material.

The preparation method in this study also could not control for post-preparation reactions of the sample surface. Material oxidation, exposure to dust, and other surface contamination was avoided to the greatest extent possible by repeating the final polishing step prior to analysis. Adsorbed water on sample surfaces was screened for and suspect nano-mechanical data excluded. However, without systematic method development, the effects of sample preparation on surface functionalization remain uncertain.

Standardizing analytical procedures is also likely critical to the success of future applications for tip-enhanced analytical methods in natural materials. The strong spectral response of organic matter documented by Yang et al. [41] and Jubb et al. [44,46] show that absorptive measurement techniques such as AFM-IR may be more suitable for strongly absorptive natural materials than reflective techniques such as IR *s*-SNOM, which rely on enough scattered light to exceed a noise threshold. The identifiable spectral features characteristic of macerals documented by Hao et al. [72] show that a very broadband light source can be advantageous, especially where peaks are broad or occupy a wide portion of the mid-IR range. However, there is typically a tradeoff between spectral bandwidth and output power, with ultra-broadband sources like synchrotrons providing limited signal strength compared to more powerful laser sources as in the present work. This study and Jakob et al. [42] have demonstrated the enhanced value of chemical information when it is paired with mechanical data. The large range of variability in the mechanical character of organic materials [47,48] suggests work is needed to establish the appropriate analytical parameters to ensure that data are being accurately recorded. For example, the rigidity modulus requires the load force to vary linearly with tip-sample separation; if the tip is too sharp, then non-linear behavior can result and values can be skewed. Finally, standardized data quality checks used in optical physics should be discussed in studies on natural materials as well. This includes ensuring that observations are not topographically correlated—a relationship which indicates that measured data are artifacts of topographic variation across a sample. This is an important and yet often overlooked issue on topographically irregular natural materials.

4.5. Future applications of tip enhanced methods to petroleum geoscience

This study highlights several fundamental advances in ultra-high resolution imaging of migrated organic matter. The strong broadband response of residual petroleum promises significant potential for future application of tip-enhanced spectroscopy in petroleum geoscience, as it demonstrates that far-field and near-field observations are compatible in geologic materials over sub-micron regions of interest. By using the infrared active regions from IR *s*-SNOM images as targets for coupled nano-mechanical data, spatial heterogeneity can be recognized in migrated material, and such data may be used to identify specific regions of interest for future analyses. The capacity for making these coupled measurements in migrated petroleum opens avenues of research that may address the implications of petroleum's mechanical character on its flow potential; on the basin-scale spatial distribution of mobile materials versus formation damaging materials; on the spatial transitions between mobile/immobile phases across thermal or lithological boundaries; and on whether intrinsic characteristics of reservoir minerals facilitate or inhibit fluid flow and phase separation. The existing studies of chemical and mechanical heterogeneity in solid organic material [e.g., [41,42,44,50]] also provide insight into how the potential production value of a petroleum resource evolves. This study demonstrates that mechanical heterogeneity in residual petroleum may be detected, which could in turn reflect nano-scale fluid dynamics that

could influence production efficiency, resource recovery, and the actualized value of the petroleum resource.

5. Conclusions

Asphaltene-based formation damage is an under-studied and problematic aspect of low permeability unconventional oil and gas reservoirs. Correlative nano-scale infrared chemical and nano-scale mechanical imaging provides a novel approach with new insight into potential heterogeneity in residual migrated petroleum where conventional analytical techniques alone fail. The mechanical data suggest the potential presence of molecular clusters and domains that differ in their adhesive force and rigidity modulus. These clusters may be due to the presence of asphaltene phase separated from maltene in pores, as is probable, given the thermodynamic constraints of reservoir conditions. That phase separation may be preferentially related to petroleum-attractive domains on calcite pore walls, and thus an intrinsic property of the coccolith debris that comprises the reservoir rock analyzed. Artifacts from sample preparation are considered as possible causes of acquired heterogeneity, and standardization of analytical techniques is encouraged for future nano-scale analyses.

In general, this study demonstrates the utility of multimodal nano-scale imaging for characterization of complex chemical systems such as petroleum in natural media. The nano-scale chemical and mechanical images in this study represent a critical step towards generating knowledge that allows incorporation of migrated and emplaced petroleum into porosity and permeability models and estimates of reservoir quality.

CRediT authorship contribution statement

Rebekah E. Simon: Conceptualization, Formal analysis, Investigation, Visualization, Writing - original draft. **Samuel C. Johnson:** Methodology, Validation, Investigation, Writing - original draft. **Omar Khatib:** Methodology, Validation, Investigation, Writing - original draft. **Markus B. Raschke:** Methodology, Supervision, Funding acquisition, Writing - review & editing. **David A. Budd:** Conceptualization, Resources, Supervision, Funding acquisition, Writing - review & editing.

Declaration of Competing Interest

The authors declare that they have no known competing financial interests or personal relationships that could have appeared to influence the work reported in this paper.

Acknowledgements

Acknowledgment is made to the Donors of the American Chemical Society Petroleum Research Fund for support of this research, and to the Rocky Mountain Association of Geologists (RMAG) Foundation for awarding R.E.S. a Norman H. Foster Memorial Scholarship. S.C.J. and M.R.B. acknowledge funding from the NSF Science and Technology Center on Real-Time Functional Imaging (STROBE) under DMR-1548924. Core samples for study were provided by the member companies of the Niobrara Pore Systems II Consortium at the University of Colorado Boulder (Budd, PI). We thank Dr. Paul C. Hackley and a second anonymous reviewer for many helpful suggestions and comments that improved the manuscript.

Appendix A. Supplementary data

Supplementary data to this article can be found online at https://doi.org/10.1016/j.fuel.2021.120836.

References

[1] Curiale JA. Origin of solid bitumens, with emphasis on biological marker results. Org Geochem 1986;10(1-3):559–80.
[2] Mastalerz M, Drobniak A, Stankiewicz AB. Origin, properties, and implications of solid bitumen in source-rock reservoirs: A review. Int J Coal Geol 2018;195:14–36.
[3] Sanei H. Genesis of solid bitumen. Sci Rep 2020;10(1). https://doi.org/10.1038/s41598-020-72692-2.
[4] Loucks RG, Reed RM, Ruppel SC, Jarvie DM. Morphology, genesis, and distribution of nanometer-scale pores in siliceous mudstones of the Mississipian Barnett Shale. J Sediment Res 2009;79:848–61.
[5] Curtis ME, Cardott BJ, Sondergeld CH, Rai CS. Development of organic porosity in the Woodford Shale with increasing thermal maturity. Int J Coal Geol 2012;103:26–31.
[6] Curtis ME, Sondergeld CH, Ambrose RJ, Rai CS. Microstructural investigation of gas shales in two and three dimensions using nanometer-scale resolution imaging. AAPG Bulletin 2012;96(4):665–77.
[7] Milliken KL, Curtis ME. Imaging pores in sedimentary rocks: Foundation of porosity prediction. Mar Pet Geol 2016;73:590–608.
[8] Milliken KL, Rudnicki M, Awwiller DN, Zhang T. Organic matter-hosted pore system, Marcellus Formation (Devonian), Pennsylvania. AAPG Bulletin 2013;97(2):177–200.
[9] Hackley PC, Cardott BJ. Application of organic petrography in North American shale petroleum systems: A review. Int J Coal Geol 2016;163:8–51.
[10] Udo OT, Etuk EE. Appliation of infrared spectroscopy for rapid petroleum source rock evaluation. J Geochem Explor 1990;37:285–300.
[11] Della Ventura G, Bellatreccia F, Marcelli A, Cestelli Guidi M, Piccinini M, Cavallo A, Piochi M. Application of micro-FTIR imaging in the Earth sciences. Anal Bioanal Chem 2010;397(6):2039–49.
[12] Dubessy J, Caumon M-C, Rull F, Sharma S. Instrumentation in Raman spectroscopy: elementary theory and practice. In: Dubessy J, Caumon M–C, Rull F, editors. Applications of raman spectroscopy to earth sciences and cultural heritage. London: European Mineralogical Union and the Mineralogical Society of Great Britain and Ireland; 2012.
[13] Ganz H, Kalkreuth W. Application of infrared spectroscopy to the classification of kerogen-types and the evaluation of source rock and oil shale potential. Fuel 1987;66:708–11.
[14] Gasaway Carley, Mastalerz Maria, Krause Fed, Clarkson Chris, Debuhr Chris. Applicability of micro-FTIR in detecting shale heterogeneity: Applicability of Micro-FTIR in detecting shale. J Microsc 2017;265(1):60–72.
[15] Nelson PH. Pore-throat sizes in sandstones, tight sandstones, and shales. AAPG Bulletin 2009;93(3):329–40.
[16] Mullins OC. The modified yen model. Energy Fuels 2010;24(4):2179–207.
[17] Yen TF. In: Structures and dynamics of asphaltenes. Boston, MA: Springer US; 1998. p. 1–20. https://doi.org/10.1007/978-1-4899-1615-0_1.
[18] Schneider MH, Andrews AB, Mitra-Kirtley S, Mullins OC. Asphaltene molecular size by fluorescence correlation spectroscopy. Energy Fuels 2007;21(5):2875–82.
[19] Mullins OC, Sabbah H, Eyssautier J, Pomerantz AE, Barré L, Andrews AB, Ruiz-Morales Y, Mostowfi F, McFarlane R, Goual L, Lepkowicz R, Cooper T, Orbulescu J, Leblanc RM, Edwards J, Zare RN. Advances in asphaltene science and the Yen–Mullins model. Energy Fuels 2012;26(7):3986–4003.
[20] Schuler B, Zhang Y, Liu F, Pomerantz AE, Andrews AB, Gross L, Pauchard V, Banerjee S, Mullins OC. Overview of asphaltene nanostructures and thermodynamic applications. Energy Fuels 2020;34(12):15082–105.
[21] Leontaritis KJ, Ali Mansoori G. Asphaltene deposition: a survey of field experiences and research approaches. J Petrol Sci Eng 1988;1(3):229–39.
[22] Soleymanzadeh A, Yousefi M, Kord S, Mohammadzadeh O. A review on methods of determining onset of asphaltene precipitation. J Petrol Explor Prod Technol 2019;9(2):1375–96.
[23] Leontaritis PhD Pres KJ. The asphaltene and wax deposition envelopes. Fuel Sci Technol Int 1996;14(1-2):13–39.
[24] Kord S, Ayatollahi S. Asphaltene precipitation in live crude oil during natural depletion: Experimental investigation and modeling. Fluid Phase Equilib 2012;336:63–70.
[25] Eyssautier J, Frot D, Barré L. Structure and dynamic properties of colloidal asphaltene aggregates. Langmuir 2012;28(33):11997–2004.
[26] Khoshandam A, Alamdari A. Kinetics of asphaltene precipitation in a heptane–toluene mixture. Energy Fuels 2010;24(3):1917–24.
[27] Mendoza de la Cruz JL, Argüelles-Vivas FJ, Matías-Pérez V, Durán-Valencia CdLA, López-Ramírez S. Asphaltene-induced precipitation and deposition during pressure depletion on a porous medium: An experimental investigation and modeling approach. Energy Fuels 2009;23(11):5611–25.
[28] Nasri Z, Dabir B. Network modeling of asphaltene deposition during two-phase flow in carbonate. J Petrol Sci Eng 2014;116:124–35.
[29] Fogden A, Olson T, Christy AG. In: Imaging unconventional reservoir pore systems. American Association of Petroleum Geologists; 2016. p. 25–42. https://doi.org/10.1306/13592015M1121402.
[30] Shen Z, Sheng JJ. Experimental study of permeability reduction and pore size distribution change due to asphaltene deposition during CO_2 huff and puff injection in Eagle Ford shale : Permeability Reduction due to Asphaltene Deposition. Asia-Pac J Chem Eng 2017;12(3):381–90.
[31] Moghanloo RG, Davudov D, Akita E. Formation damage by organic deposition. In: Yuan B, Wood DA, editors. Formation damage during improved oil recovery: Fundamentals and applications. Gulf Professional Publishing (Elsevier); 2018. p. 676.

[32] Dazzi A, Prazeres R, Glotin F, Ortega JM. Local infrared microspectroscopy with subwavelength spatial resolution with an atomic force microscope tip used as a photothermal sensor. Opt. Lett. 2005;30(18):2388. https://doi.org/10.1364/OL.30.002388.

[33] Nowak D, Morrison W, Wickramasinghe HK, Jahng J, Potma E, Wan L, Ruiz R, Albrecht TR, Schmidt K, Frommer J, Sanders DP, Park S. Nanoscale chemical imaging by photoinduced force microscopy. Sci. Adv. 2016;2(3):e1501571. https://doi.org/10.1126/sciadv.1501571.

[34] Richards D, Zayats A, Keilmann F, Hillenbrand R. Near-field microscopy by elastic light scattering from a tip. Philos Trans R Soc London, Ser A 2004;362(1817):787–805.

[35] Atkin JM, Berweger S, Jones AC, Raschke MB. Nano-optical imaging and spectroscopy of order, phases, and domains in complex solids. Adv Phys 2012;61(6):745–842.

[36] Chen X, Hu D, Mescall R, You G, Basov DN, Dai Q, et al. Modern scattering-type scanning near-field optical microscopy for advanced material research. Adv Mater 2019;31(24):1804774.

[37] Muller EA, Pollard B, Raschke MB. Infrared chemical nano-imaging: Accessing structure, coupling and dynamics on molecular length scales. J Phys Chem Lett 2015;6:1275–84.

[38] Pollard B, Raschke MB. Correlative infrared nanospectroscopic and nanomechanical imaging of block copolymer domains. Beilstein J Nanotechnol 2016;7:605–12.

[39] Bechtel HA, Johnson SC, Khatib O, Muller EA, Raschke MB. Synchrotron infrared nano-spectroscopy and -imaging. Surf Sci Rep 2020;75(3):100493. https://doi.org/10.1016/j.surfrep.2020.100493.

[40] Wang Le, Wang H, Wagner M, Yan Y, Jakob DS, Xu XG. Nanoscale simultaneous chemical and mechanical imaging via peak force infrared microscopy. Sci Adv 2017;3(6):e1700255. https://doi.org/10.1126/sciadv.1700255.

[41] Yang J, Hatcherian J, Hackley PC, Pomerantz AE. Nanoscale geochemical and geomechanical characterization of organic matter in shale. Nat Commun 2017;8(1). https://doi.org/10.1038/s41467-017-02254-0.

[42] Jakob DS, Wang Le, Wang H, Xu XG. Spectro-mechanical characterizations of kerogen heterogeneity and mechanical properties of source rocks at 6 nm spatial resolution. Anal Chem 2019;91(14):8883–90.

[43] Abarghani A, Gentzis T, Shokouhimehr M, Liu Bo, Ostadhassan M. Chemical heterogeneity of organic matter at nanoscale by AFM-based IR spectroscopy. Fuel 2020;261:116454. https://doi.org/10.1016/j.fuel.2019.116454.

[44] Jubb AM, Birdwell JE, Hackley PC, Hatcherian JJ, Qu J. Nanoscale molecular composition of solid bitumen from the eagle ford group across a natural thermal maturity gradient. Energy Fuels 2020;34(7):8167–77.

[45] Jubb AM, Hackley PC, Birdwell JE, Hatcherian J, Qu J. Examination of intertinite within immature Eagle Ford Shale at the nanometer-scale using atomic force microscopy-based infrared spectroscopy. Int J Coal Geol 2020;231:103608.

[46] Jubb AM, Hackley PC, Hatcherian JJ, Qu J, Nesheim TO. Nanoscale molecular fractionation of organic matter within unconventional petroleum source beds. Energy Fuels 2019;33(10):9759–66.

[47] Li C, Ostadhassan M, Gentzis T, Kong L, Carvajal-Ortiz H, Bubach B. Nanomechanical characterization of organic matter in the Bakken formation by microscopy-based method. Mar Pet Geol 2018;96:128–38.

[48] Li C, Ostadhassan M, Guo S, Gentzis T, Kong L. Application of the PeakForce tapping mode of atomic force microscope to characterize nanomechanical properties of organic matter of the Bakken Shale. Fuel 2018;233:894–910.

[49] Tian S, Dong X, Wang T, Zhang R, Zhang P, Sheng M, Cheng S, Zhao H, Fei L, Street J, Chen Y, Xu Q. Surface properties of organic kerogen in continental and marine shale. Langmuir 2018;34(46):13882–7.

[50] Tian S, Wang T, Li G, Sheng M, Zhang P. Nanoscale surface properties of organic matter and clay minerals in shale. Langmuir 2019;35(17):5711–8.

[51] Kauffman EG. Upper Cretaceous cyclothems, biotas, and environments, Rock Canyon Anticline, Pueblo. Colorado. The Mountain Geologist 1977;14:129–52.

[52] Kauffman EG, Caldwell WGE. The Western Interior Basin in space and time. In: Caldwell WGE, Kauffman EG, editors. Evolution of the Western Interior Basin. Geological Association of Canada; 1993. p. 397–434.

[53] Pratt LM, Barlow LK. Isotopic and sedimentological study of the lower Niobrara Formation, Lyons, Colorado. In: Pratt LM, Kauffman EG, Zelt FB, editors. Fine-grained Deposits and Biofacies of the Cretaceous Western Interior Seaway: Evidence of Cyclic Sedimentary Processes. Society of Economic Paleontologists and Mineralogists; 1985, p. 209-14.

[54] Longman M. Revisiting the upper cretaceous Niobrara petroleum system in the Rocky Mountain region. The Mountain Geologist 2020;57(2):45–66.

[55] Longman MW, Luneau BA, Landon SM. Nature and distribution of Niobrara lithologies in the Cretaceous Western Interior Seaway of the Rocky Mountain region. The Mountain Geologist 1998;35:137–70.

[56] Zhang S, Canter L, Sonnenfeld M. Capillary fluid dynamics within unconventional rocks investigated by scanning electron microscopy. AAPG Bulletin 2017;101(11):1759–65.

[57] Canter L, Zhang S, Sonnenfeld M, Bugge C, Guisinger M, Jones K. In: Imaging unconventional reservoir pore systems. American Association of Petroleum Geologists; 2016. p. 9–23. https://doi.org/10.1306/13592014M1123691.

[58] Han Y, Horsfield B, LaReau H, Mahlstedt N. Intraformational migration of petroleum: Insights into the development of sweet spot in the Cretaceous Niobrara shale-oil system, Denver Basin. Mar Pet Geol 2019;107:301–9.

[59] Larter S. Some pragmatic perspectives in source rock geochemistry. Mar Pet Geol 1988;5(3):194–204.

[60] Boudinot FG, Dildar N, Leckie RM, Parker A, Jones MM, Sageman B, et al. Neritic ecosystem response to Oceanic Anoxic Event 2 in the Cretaceous Western Interior Seaway. Palaeogeogr Palaeoclimatol Palaeoecol 2020;546:12.

[61] Simon RE. Integrating the Effects of Diagenesis and Catagenesis on Pore Network Evolution in an Unconventional Chalk Reservoir: Cretaceous Niobrara Formation, Colorado, USA. Department of Geological Sciences. Doctor of Philosophy. Boulder, CO: University of Colorado Boulder; 2020.

[62] Amenabar I, Poly S, Goikoetxea M, Nuansing W, Lasch P, Hillenbrand R. Hyperspectral infrared nanoimaging of organic samples based on Fourier transform infrared nanospectroscopy. Nat Commun 2017;8(1). https://doi.org/10.1038/ncomms14402.

[63] Pittenger B, Erina N, Su C. Mechanical property mapping at the nanoscale using PeakForce QNM Scanning Probe Technique. In: Tiwari A, editor. Nanomechanical analysis of high performance materials. Springer; 2014. p. 31–52.

[64] Gwyddion.. 2.48 ed.: Department of Nanometrology. Czech Metrology Institute 2017.

[65] Coates J. Interpretation of infrared spectra, A practical approach. In: Meyers RA, editor. Encyclopedia of Analytical Chemistry. Chichester, UK: Wiley; 2000. p. 10815–37.

[66] Mester L, Govyadinov AA, Chen S, Goikoetxea M, Hillenbrand R. Subsurface chemical nanoidentification by nano-FTIR spectroscopy. Nat Commun 2020;11(1). https://doi.org/10.1038/s41467-020-17034-6.

[67] Andrews AB, Wang D, Marzec KM, Mullins OC, Crozier KB. Surface enhanced Raman spectroscopy of polycyclic aromatic hydrocarbons and molecular asphaltenes. Chem Phys Lett 2015;620:139–43.

[68] Tissot BP, Welte DH, editors. Petroleum formation and occurrence. Berlin, Heidelberg: Springer Berlin Heidelberg; 1984.

[69] Pernyeszi T, Patzko A, Berkesi O, Dekany I. Asphaltene adsorption on clays and crude oil reservoirs. Colloids Surf A 1998;137:373–84.

[70] Dudášová D, Simon Sébastien, Hemmingsen PÅlV, Sjöblom J. Study of asphaltenes adsorption onto different minerals and clays. Colloids Surf, A 2008;317(1–3):1–9.

[71] Landon SM, Longman MW, Luneau BA. Hydrocarbon source rock potential of the upper cretaceous Niobrara Formation, Western Interior Seaway of the Rocky Mountain region. The Mountain Geologist 2001;38:1–18.

[72] Hao Z, Bechtel HA, Kneafsey T, Gilbert B, Nico PS. Cross-scale molecular analysis of chemical heterogeneity in shale rocks. Sci Rep 2018;8(1). https://doi.org/10.1038/s41598-018-20365-6.

[73] Eberhardsteiner L, Füssl J, Hofko B, Handle F, Hospodka M, Blab R, et al. Influence of asphaltene content on mechanical bitument behavior: experimental investigation and micromechanical modeling. Mater Struct 2015;48:3099–112.

[74] Masson J-F, Leblond V, Margeson J. Bitumen morphologies by phase-detection atomic force microscopy. J Microsc 2006;221(1):17–29.

[75] Lyne ÅsaL, Wallqvist V, Birgisson B. Adhesive surface characteristics of bitumen binders investigated by Atomic Force Microscopy. Fuel 2013;113:248–56.

[76] Hassenkam T, Skovbjerg LL, Stipp SLS. Probing the intrinsically oil-wet surfaces of pores in North Sea chalk at subpore resolution. Proceedings of the National Academy of Sciences 2009;106:6071-6.

[77] Kim S, Jeong Park M, Balsara NP, Liu G, Minor AM. Minimization of focused ion beam damage in nanostructured polymer thin films. Ultramicroscopy 2011;111(3):191–9.

[78] Sanei H, Ardakani OH. Alteration of organic matter by ion milling. Int J Coal Geol 2016;163:123–31.

[79] Mastalerz M, Schieber J. Effect of ion milling on the perceived maturity of shale samples: Implications for organic petrography and SEM analysis. Int J Coal Geol 2017;183:110–9.

[80] Katz BJ, Arango I. Organic porosity: A geochemist's view of the current state of understanding. Org Geochem 2018;123:1–16.

[81] Hackley PC, Jubb AM, Valentine BJ, Hatcherian JJ, Yu J-J, Podrazky WK. Investigating the effects of broad ion beam milling to sedimentary organic matter: Surface flattening or heat-induced aromatization and condensation? Fuel 2020;282:118627. https://doi.org/10.1016/j.fuel.2020.118627.

[82] Michaels J, Budd D. Pore systems of the B-chalk zone in the Niobrara Formation, Denver-Julesburg Basin, Colorado. Unconventional Resources Technology Conference (URTeC). Denver, CO; 2014.